The inverse problem for conducting defective lattices

Vikram Bhamidipati[a], Loukas F. Kallivokas[b,c,*], Gregory J. Rodin[a,c]

[a] *Aerospace Engineering and Engineering Mechanics, The University of Texas at Austin, United States of America*
[b] *Civil, Architectural and Environmental Engineering, The University of Texas at Austin, United States of America*
[c] *Oden Institute for Computational Engineering and Sciences, The University of Texas at Austin, Austin, TX 78712, United States of America*

Abstract

We are concerned with the inverse problem of detecting and localizing defects in finite lattices. Using polarization dipoles applied at the ends of defective bars, the forward problem for a defective lattice is cast on the underlying pristine lattice. As a result, the inverse problem of localizing lattice defects is reduced to an inverse source problem, in which the inversion variables are the polarization dipoles representing defective bars, while all computations are carried out on the pristine lattice. We present the forward and inverse problem formulations, propose an algorithm for solving the inverse problem, and report results of numerical experiments driven by either complete or incomplete boundary data.
© 2022 Elsevier B.V. All rights reserved.

1. Introduction

Advances in additive manufacturing have created multiple opportunities for manufactured lattices (meta-materials) with interesting and useful properties [1–3]. Analysis, design, and optimization of these lattices accentuates the need for computational methods that take advantage of lattice periodicity and discreteness.

In this article, we are concerned with localizing defects in conducting lattices. While conduction problems are convenient for describing our approach, the methodology can be extended to other lattices, most notably to mechanical lattices. We restrict our attention to defective lattices formed upon removal of bars from otherwise pristine periodic lattices. Accordingly, our goal is to locate the removed bars, using complete or incomplete data for nodal temperatures and/or sources measured on the lattice boundary. This is a discrete inverse problem. In the continuum setting, detection of interior voids from boundary data, and, more broadly, thermal inverse problems, have received considerable attention (see, for example, [4–6]). In contrast, the literature on inverse problems for conducting lattices is primarily concerned with various challenging mathematical aspects rather than applications (e.g., [7]).

In the continuum case, inverse problems involving localization of defects are often solved in two steps: (i) one determines position-dependent properties of the entire medium, and (ii) defects are inferred from property gradients. This process is iterative, as the responses corresponding to trial property distributions are compared against the

---

measurements, until the misfit between predicted and measured responses is minimized in a suitable norm. Since the properties change at every inversion iteration, the underlying discretization may have to be changed throughout the process. If a similar approach is adopted for defective lattices, then the inversion iterations would involve lattices whose defects, and, consequently, the topology, change from one iteration to another — a computationally undesirable strategy.

In this article, we build upon the approach for the forward problem for defective conducting lattices of arbitrary topology and periodicity developed in [8–13]. In that approach, first, each removed bar is returned back into the lattice, so that the underlying pristine lattice is formed. Second, for each returned bar in the pristine lattice, a polarization dipole of sources applied at the bar nodes is introduced. Third, the polarization dipoles are computed so that the returned bars operate as removed bars, that is, conduct no heat. Accordingly, in the process of solving the inverse problem, there is no need to explicitly account for topological changes of the lattice. Rather, one has to track the polarization dipoles applied in the same pristine lattice. Thus, the inverse *medium* problem defined over the topologically changing lattice is recast as an inverse *source* problem over the pristine lattice.

We address the inverse source problem as a model-constrained optimization problem, following steps similar to partial-differential-equation-constrained optimization approaches used in continuum inverse problems [14]; for various applications we refer to [15–17]. There, the Lagrangian functional to be minimized consists of three terms: a misfit (difference between predicted and measured data), the side imposition of the forward problem, and a regularization term aimed at alleviating solution multiplicity. In our approach, the misfit term is constructed in a manner that ensures the satisfaction of the forward problem *a priori*, while the regularization term deviates from either the standard Tikhonov or Total Variation ansatz.

The remainder of the article is organized as follows. In Section 2, we briefly review the forward problem for defective lattices, and use numerical experiments to demonstrate that the boundary data are rather insensitive to a defect's location in the lattice. This motivates us to replace the original forward problem with an equivalent perturbation problem, whose boundary data are more sensitive to the defect; this is done in Section 3. In Section 4, we develop a two-stage algorithm for solving the inverse problem. In Section 5, we present results of numerical experiments for various defective lattices, based on synthetic measurements for both complete and incomplete Cauchy data. In Section 6, we conclude with remarks on the effectiveness of the proposed approach to the inverse problem for conducting defective lattices.

2. The forward problem

Consider an infinite conducting simple square lattice $\mathcal{L}^\infty$ formed by identical bars of length h and conductance c (Fig. 1). Following [13], we impose on $\mathcal{L}^\infty$ a square contour Γ, so that the bars entirely inside Γ form a lattice plate of size $nh \times nh$. We refer to this plate as $\mathcal{L}$ and denote its bars by $\mathcal{B}$ and its nodes by $\mathcal{N}$. The nodes along the edges of $\mathcal{L}$ are defined as exterior and denoted by $\mathcal{N}_e$, and the remaining nodes of $\mathcal{L}$ are defined as interior and denoted by $\mathcal{N}_i$.

By construction,

$$N := \dim \mathcal{N} = (n+1)^2, \quad N_e := \dim \mathcal{N}_e = 4n, \quad \text{and} \quad N_i := \dim \mathcal{N}_i = (n-1)^2.$$

Conventionally, a thermal state of a conducting lattice is characterized by column-vectors of nodal temperatures $\mathbf{u}$ and sources $\mathbf{f}$ related by the conductance matrix $\mathbf{C}$:

$$\mathbf{Cu} = \mathbf{f}. \tag{1}$$

This $N \times N$ matrix is formed by applying the standard five-point stencil at every interior node, and truncated stencils at the exterior nodes. In a typical forward problem, at each node $i \in \mathcal{N}$, either $u(i)$ or $f(i)$ is prescribed, for a total of N prescribed components, and (1) can be used to solve for the remaining N components. This problem has a unique solution, provided that at least one nodal temperature is prescribed. This assumption is not critical for our development, but we will adopt it as it simplifies the presentation.

Here, we follow [13] and replace (1) with an equivalent system of equations derived with the aid of the reciprocity theorem and the lattice Green's function G for $\mathcal{L}^\infty$ [18]:

$$u(i) + \sum_{j \in \mathcal{N}_e} \sum_{k \in \bar{\mathcal{N}}(j)} c\left[G(k, i) - G(j, i)\right] u(j) = \sum_{j \in \mathcal{N}} G(j, i) f(j) \quad i \in \mathcal{N}. \tag{2}$$
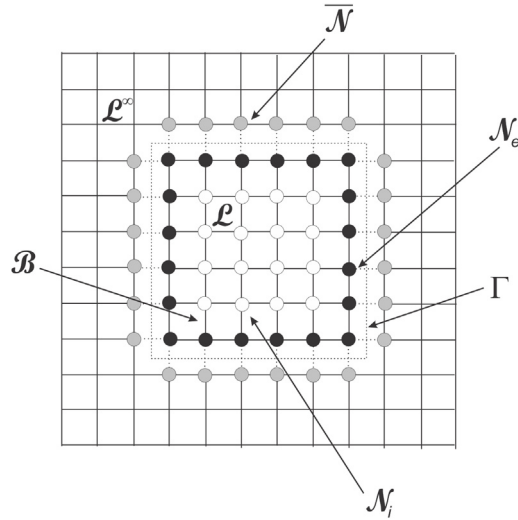
Fig. 1. Schematic of lattice geometry $\mathcal{L}$ and related node sets.

In this equation, i, j, and k are integer pairs, each representing nodal Cartesian coordinates normalized by the lattice spacing h. The node set $\bar{\mathcal{N}}(j)$ consists of all nodes *exterior* to $\mathcal{N}$, which are directly connected to $j \in \mathcal{N}_e$ (Fig. 1).

The main reason for choosing (2) over (1) is because it is well-suited for analyzing defective lattices. Such a defective lattice is formed by removing a few bars from the pristine lattice $\mathcal{L}$. The defective lattice can be also viewed as the pristine lattice in which some of the bars are assigned zero conductance. This perspective is particularly useful for our approach, as the pristine and defective lattices can be regarded as geometrically and topologically identical.

A defective bar α is simulated with a polarization dipole, defined by the sources $\mu(\alpha)$ and $-\mu(\alpha)$, applied at the end nodes of the bar in the pristine lattice. The polarization sources, representing a set of defective bars $\mathcal{B}_\mu$, can be simply regarded as additional nodal sources applied in the pristine lattice. These sources are expressed as

$$f(i) = \sum_{\alpha \in \mathcal{B}_\mu} \mu(\alpha) \left[\delta(i, \alpha^+) - \delta(i, \alpha^-) \right] \quad i \in \mathcal{N}, \tag{3}$$

where δ is the Kronecker symbol, and α^+ and α^- denote the end nodes of bar α.

In the presence of the polarization sources, (2) is modified, so that it includes the additional term due to the sources defined in (3):

$$u(i) + \sum_{j \in \mathcal{N}_e} \sum_{k \in \bar{\mathcal{N}}(j)} c \left[G(k, i) - G(j, i) \right] u(j) =$$
$$\sum_{j \in \mathcal{N}} G(j, i) f(j) + \sum_{\beta \in \mathcal{B}_\mu} \left[G(i, \beta^+) - G(i, \beta^-) \right] \mu(\beta) \quad i \in \mathcal{N}. \tag{4}$$

This expression describes N equations relating $2N + N_\mu$ unknowns, where

$$N_\mu := \dim \mathcal{B}_\mu. \tag{5}$$

The unknowns comprise N nodal temperatures, N nodal sources, and N_μ polarization dipoles. Thus, provided that N components of either **u** or **f** are prescribed, the system of N equations in (4) alone is not sufficient for determining the remaining $N + N_\mu$ unknowns. This necessitates the introduction of additional N_μ equations, which, as it will be shown, establish the equivalence between defective bars of zero conductance and the corresponding polarization dipoles.

The thermal flux flowing through a defective bar with zero conductance must equal zero. This condition can be stated by considering a pristine bar subjected to the polarization sources $\mu(\alpha)$ and $-\mu(\alpha)$ at the nodes α^+ and α^-,

respectively. Then the total thermal flux flowing through the pristine bar involves the polarization flux $\mu(\alpha)$ and the usual thermal flux. As a result, the equivalence condition for the defective bar α is stated in the form

$$\mu(\alpha) + c\left[u(\alpha^+) - u(\alpha^-)\right] = 0 . \tag{6}$$

It is expedient to formulate N_μ equations equivalent to (6) in a manner similar to (4). To this end, we evaluate (4) at the nodes α^+ and α^-, and combine the resulting two equations with (6) to obtain the sought N_μ equations:

$$
\begin{aligned}
-\frac{\mu(\alpha)}{c} + & \\
\sum_{j\in\mathcal{N}_e}\sum_{k\in\hat{\mathcal{N}}(j)} c\left[G(k,\alpha^+) - G(j,\alpha^+) - G(k,\alpha^-) + G(j,\alpha^-)\right]u(j) = & \\
\sum_{j\in\mathcal{N}}\left[G(j,\alpha^+) - G(j,\alpha^-)\right]f(j) + & \\
\sum_{\beta\in\mathcal{B}_\mu}\left[G(\beta^+,\alpha^+) - G(\beta^-,\alpha^+) - G(\beta^+,\alpha^-) + G(\beta^-,\alpha^-)\right]\mu(\beta), \quad \alpha\in\mathcal{B}_\mu .
\end{aligned}
\tag{7}
$$

The $N + N_\mu$ equations (4) and (7) can now be used to analyze defective lattices in the same manner as (2) can be used for analyzing pristine lattices. Let us stress that the *operations implied by* (4) *and* (7) *are defined on the pristine lattice*: no topological modification of the lattice to account for defective bars is needed.

Next, we restrict our attention to a class of problems for defective lattices characterized by the prescription

$$f(i) = 0, \quad i\in\mathcal{N}_i . \tag{8}$$

With this provision, (4) and (7) can be recast by simply replacing all occurrences of the set $\mathcal{N}$ with the set $\mathcal{N}_e$. The resulting system consists of $N_e + N_\mu$ equations for $2N_e + N_\mu$ unknowns, i.e., N_e nodal temperatures, N_e nodal sources, and N_μ polarization dipoles. We express the system in the symbolic form

$$
\begin{bmatrix} \mathbf{I}+\mathbf{K} & -\mathbf{V} & -\mathbf{L} \\ -\mathbf{M}^* & \mathbf{L}^* & \mathbf{N} \end{bmatrix}
\begin{Bmatrix} \mathbf{u}_e \\ \mathbf{f}_e \\ \boldsymbol{\mu} \end{Bmatrix} = \mathbf{0} .
\tag{9}
$$

Here $\mathbf{u}_e$ and $\mathbf{f}_e$ are the column-vectors of nodal temperatures $u(i)$ and sources $f(i)$, respectively, with $i\in\mathcal{N}_e$, and $\boldsymbol{\mu}$ is the column-vector of polarization dipoles $\mu(\alpha)$, with $\alpha\in\mathcal{B}_\mu$. The block-matrices in (9) are defined as follows:

$$
\begin{aligned}
K(i,j) &:= \sum_{k\in\bar{\mathcal{N}}(j)} c\left[G(k,i) - G(j,i)\right] , \\
V(i,j) &:= G(j,i) , \\
L(i,\beta) &:= G(i,\beta^+) - G(i,\beta^-) , \\
M(\alpha,j) &:= -\sum_{k\in\hat{\mathcal{N}}(j)} c\left[G(k,\alpha^+) - G(j,\alpha^+) - G(k,\alpha^-) + G(j,\alpha^-)\right] , \\
N(\alpha,\beta) &:= -\frac{\delta(\alpha,\beta)}{c} - \left[G(\beta^+,\alpha^+) - G(\beta^-,\alpha^+) - G(\beta^+,\alpha^-) + G(\beta^-,\alpha^-)\right] .
\end{aligned}
$$

In (9), $\mathbf{L}^*$ denotes the adjoint of $\mathbf{L}$, and $\mathbf{I}$ is the identity matrix. Further, it is useful to identify these matrices in (9) as maps:

$$
\begin{aligned}
\mathbf{I}+\mathbf{K}, \mathbf{V} &: \mathcal{N}_e \to \mathcal{N}_e , \\
\mathbf{L} &: \mathcal{B}_\mu \to \mathcal{N}_e , \\
\mathbf{M}^* &: \mathcal{N}_e \to \mathcal{B}_\mu , \\
\mathbf{N} &: \mathcal{B}_\mu \to \mathcal{B}_\mu .
\end{aligned}
\tag{10}
$$

For further details pertaining to (9) we refer to [13].

Provided that at every external node $i\in\mathcal{N}_e$ either the temperature or the source is prescribed (for a total of N_e prescribed components), (9) can be solved for the remaining $N_e + N_\mu$ components. By appealing to an analogy with the continuum case, we demand, in effect, that half of the Cauchy data be prescribed on the lattice boundary,
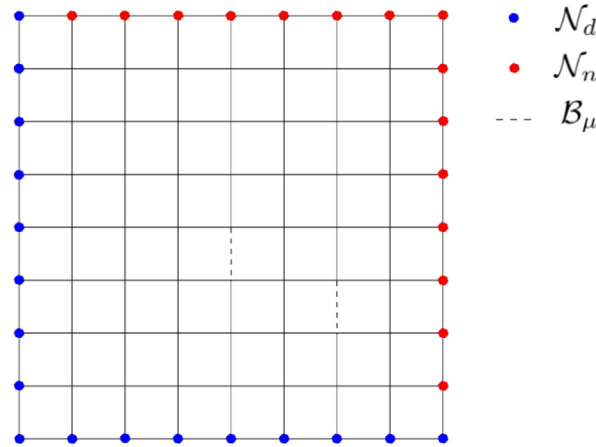
Fig. 2. Schematic of a defective lattice: defective bars (set $\mathcal{B}_\mu$) are shown with dotted lines. Nodal data partitions $\mathcal{N}_d$ and $\mathcal{N}_n$ are shown with blue and red solid circles, respectively. (For interpretation of the references to color in this figure legend, the reader is referred to the web version of this article.)

in order to be able to solve for the remaining Cauchy data and the polarization dipoles. Consider, for example, a partition of the exterior node set $\mathcal{N}_e$ into a set $\mathcal{N}_d$, where nodal temperatures are prescribed, and a set $\mathcal{N}_n$, where nodal sources are prescribed. The nodal partitions are such that $\mathcal{N}_e = \mathcal{N}_d \cup \mathcal{N}_n$ and $\mathcal{N}_d \cap \mathcal{N}_n = \emptyset$ (Fig. 2). The subscripts d and n refer to Dirichlet and Neumann, respectively, and we will extend their use to column-vectors and matrices.

Let the prescribed data be

$$
\begin{aligned}
u(i) &= \phi(i), \quad i \in \mathcal{N}_d \,, \ \text{or } \mathbf{u}_d = \boldsymbol{\phi} \,, \\
f(i) &= \psi(i), \quad i \in \mathcal{N}_n \,, \ \text{or } \mathbf{f}_n = \boldsymbol{\psi} \,.
\end{aligned}
\tag{11}
$$

Accordingly, we can first recast (9) as,

$$
\begin{bmatrix}
(\mathbf{I}+\mathbf{K})_{dd} & \mathbf{K}_{dn} & -\mathbf{V}_{dd} & -\mathbf{V}_{dn} & -\mathbf{L}_{d\mu} \\
\mathbf{K}_{nd} & (\mathbf{I}+\mathbf{K})_{nn} & -\mathbf{V}_{nd} & -\mathbf{V}_{nn} & -\mathbf{L}_{n\mu} \\
-\mathbf{M}^*_{\mu d} & -\mathbf{M}^*_{\mu n} & \mathbf{L}^*_{\mu d} & \mathbf{L}^*_{\mu n} & \mathbf{N}_{\mu\mu}
\end{bmatrix}
\begin{Bmatrix}
\mathbf{u}_d \\ \mathbf{u}_n \\ \mathbf{f}_d \\ \mathbf{f}_n \\ \boldsymbol{\mu}
\end{Bmatrix}
= \mathbf{0} \,,
\tag{12}
$$

and then combine it with (11) to obtain:

$$
\begin{bmatrix}
(\mathbf{I}+\mathbf{K})_{nn} & -\mathbf{V}_{nd} & -\mathbf{L}_{n\mu} \\
-\mathbf{M}^*_{\mu n} & \mathbf{L}^*_{\mu d} & \mathbf{N}_{\mu\mu}
\end{bmatrix}
\begin{Bmatrix}
\mathbf{u}_n \\ \mathbf{f}_d \\ \boldsymbol{\mu}
\end{Bmatrix}
=
\begin{bmatrix}
-\mathbf{K}_{nd} & \mathbf{V}_{nn} \\
\mathbf{M}^*_{\mu d} & -\mathbf{L}^*_{\mu n}
\end{bmatrix}
\begin{Bmatrix}
\boldsymbol{\phi} \\ \boldsymbol{\psi}
\end{Bmatrix} \,.
\tag{13}
$$

We regard this system of equations for the unknowns $\mathbf{u}_n$, $\mathbf{f}_d$, and $\boldsymbol{\mu}$ as the statement of the forward problem for defective lattices.

3. The perturbation problem

In the inverse problem, in addition to the prescribed data $\boldsymbol{\phi}$ and $\boldsymbol{\psi}$, a few components of $\mathbf{u}_n$ and/or $\mathbf{f}_d$ are measured, and, thus, become known. If all of the components of $\mathbf{u}_n$ and $\mathbf{f}_d$ are known, we refer to the data as the *complete* Cauchy data. Otherwise, the data are *incomplete*. The objective of the inverse problem is to solve (13) for $\boldsymbol{\mu}$ for known Cauchy data, whether complete or incomplete.

In addition to the usual challenges associated with inverse problems, we discovered that using (13) is particularly challenging because the Cauchy data turned out to be rather insensitive to defect location, as we demonstrate in Section 3.1. To address this issue, in Section 3.2, we formulate a perturbation problem equivalent to (13), which exhibits much better sensitivity of the Cauchy data to the defect location.
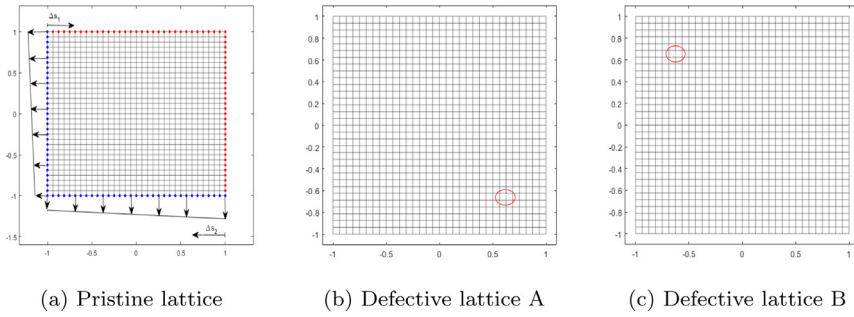
(a) Pristine lattice   (b) Defective lattice A   (c) Defective lattice B

Fig. 3. Lattice geometry: (a) Pristine lattice; (b) First defective lattice with the removed bar in the bottom-right quadrant; (c) Second defective lattice with the removed bar in the top-left quadrant. (For interpretation of the references to color in this figure legend, the reader is referred to the web version of this article.)
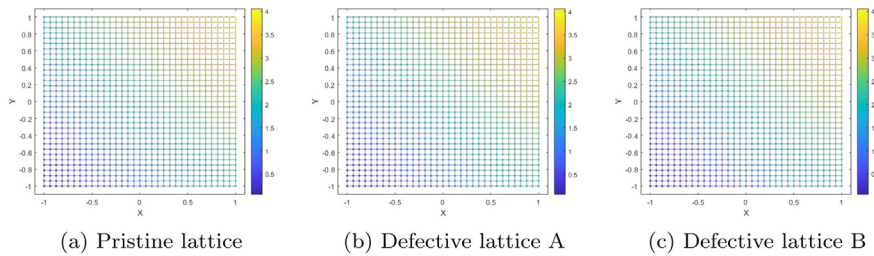

(a) Pristine lattice   (b) Defective lattice A   (c) Defective lattice B

Fig. 4. Temperature distribution for the pristine and two defective lattices. (For interpretation of the references to color in this figure legend, the reader is referred to the web version of this article.)

3.1. A motivational example

Consider a pristine square lattice plate that occupies the domain $-1 \leq x, y \leq 1$, and consists of identical bars of length $h = 1/16$. Accordingly, for this lattice, $n = 32$, the total number of lattice nodes is $N = 33^2$, and the lattice boundary comprises $N_e = 128$ nodes. The pristine lattice is shown in Fig. 3a; Fig. 3b and c show two different defective lattices, each formed by removing a single vertical bar. For the first defective lattice (Fig. 3b), that bar is $x = 10h, -11h < y < -10h$, and, for the second defective lattice (Fig. 3c) the removed bar is $x = -10h, 10h < y < 11h$. The induced thermal states are such that each node along the top and right edges is subjected to a unit source (Fig. 3a). Thus $\mathcal{N}_n = \{i : (x_i, y_i) \in \{(-15h \dots 15h, 1)\} \cup \{1, (-15h \dots 1)\}\}$, and the number of nodes where the sources are prescribed is equal to 63. Further, the nodes on the left edge ($x = -1, -1 \leq y \leq h$ are assigned linearly-varying temperatures from 0.0625 to 2.0, such that $u(-1, -15h) = 1/16$ and $u(-1, 1) = 2$. Similarly, the nodes on the bottom edge $-1 \leq x \leq 1, y = -1$ are also assigned linearly-varying temperatures such that $u(-1, -1) = 1/16$ and $u(1, -1) = 33/16$. The total number of nodes where the temperatures are prescribed is equal to 65.

Next, (13) is solved for the three lattices shown in Fig. 3. For the pristine lattice, the solution is for the remaining $N_e = 128$ components of the Cauchy data; the polarization dipole is set equal to zero. For each defective lattice, the solution involves the remaining Cauchy data and the polarization dipole. Once (13) has been solved, the nodal temperatures in the interior are computed using (4) for $i \in \mathcal{N}_i$. The results for all three lattices are shown as contour plots in Fig. 4: as it can be seen, there are no visually discernible differences among the three cases, despite the fact that the three lattice problems are not the same.

To get a closer look at the results, in Fig. 5 we plot the computed Cauchy data along the lattice edges. Specifically, in Fig. 5a, the nodal temperatures for all three lattices are plotted as functions of the arc-length coordinate Δs_1 along the top and right lattice edges (where the Neumann data were prescribed), and in Fig. 5b, the (reaction) sources are plotted as functions of the arc-length coordinate Δs_2 along the bottom and left lattice edges (where the Dirichlet data were prescribed). The arc-length origins for both Δs_1 and Δs_2 are shown in Fig. 3a. In both cases, the boundary is traversed clockwise. As it can be seen in Fig. 5, the presence of the defect had hardly any effect on the computed
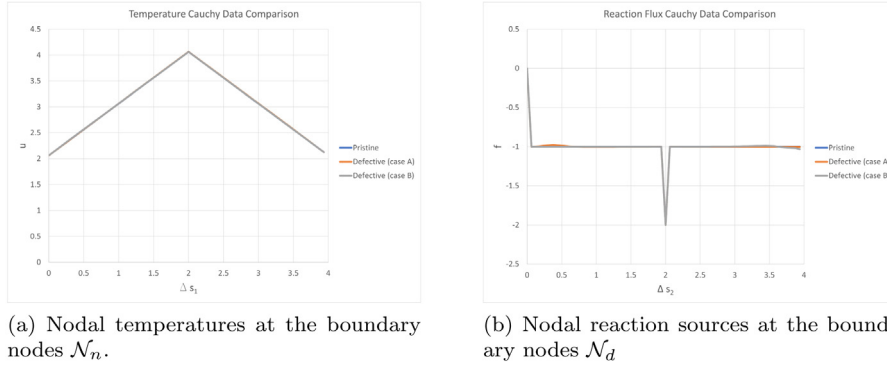
(a) Nodal temperatures at the boundary nodes $\mathcal{N}_n$.

(b) Nodal reaction sources at the boundary nodes $\mathcal{N}_d$

Fig. 5. The nodal temperatures and reaction sources along the lattice boundary for the pristine and two defective lattices. (For interpretation of the references to color in this figure legend, the reader is referred to the web version of this article.)

Dirichlet data (Fig. 5a), whereas the effect of the defect was highly localized for the computed Neumann data (Fig. 5b).

Results presented in Figs. 4 and 5 are characteristic of other pristine and defective lattices, and suggest that the Cauchy data are rather insensitive not only to defect location but even to defect presence. Since defect detection is driven by Cauchy data, it is imperative to improve the sensitivity. To this end, in the next subsection we reformulate the forward problem in a way that appears to achieve this objective.

3.2. Problem formulation

The perturbation forward problem is formulated for the difference between solutions of two problems. The first problem is for the defective lattice and data $\boldsymbol{\phi}$ and $\boldsymbol{\psi}$. The second problem involves the same data but the pristine, rather than the defective lattice. Thus, the perturbation forward problem is characterized by zero prescribed boundary data, and its solution is driven by the polarization dipoles. Schematically, this is shown in Fig. 6.

Mathematically, the perturbation problem is formulated by specifying (12) for both defective and pristine lattices. Accordingly, for the defective lattice we obtain

$$
\begin{bmatrix}
(\mathbf{I}+\mathbf{K})_{dd} & \mathbf{K}_{dn} & -\mathbf{V}_{dd} & -\mathbf{V}_{dn} & -\mathbf{L}_{d\mu} \\
\mathbf{K}_{nd} & (\mathbf{I}+\mathbf{K})_{nn} & -\mathbf{V}_{nd} & -\mathbf{V}_{nn} & -\mathbf{L}_{n\mu} \\
-\mathbf{M}^*_{\mu d} & -\mathbf{M}^*_{\mu n} & \mathbf{L}^*_{\mu d} & \mathbf{L}^*_{\mu n} & \mathbf{N}_{\mu\mu}
\end{bmatrix}
\begin{Bmatrix}
\boldsymbol{\phi} \\
\mathbf{u}_n^{(D)} \\
\mathbf{f}_d^{(D)} \\
\boldsymbol{\psi} \\
\boldsymbol{\mu}
\end{Bmatrix}
= \mathbf{0} .
\tag{14}
$$

For the pristine lattice, the last row of the block-matrix is omitted because the polarization dipoles are not involved, and therefore (12) yields

$$
\begin{bmatrix}
(\mathbf{I}+\mathbf{K})_{dd} & \mathbf{K}_{dn} & -\mathbf{V}_{dd} & -\mathbf{V}_{dn} \\
\mathbf{K}_{nd} & (\mathbf{I}+\mathbf{K})_{nn} & -\mathbf{V}_{nd} & -\mathbf{V}_{nn}
\end{bmatrix}
\begin{Bmatrix}
\boldsymbol{\phi} \\
\mathbf{u}_n^{(P)} \\
\mathbf{f}_d^{(P)} \\
\boldsymbol{\psi}
\end{Bmatrix}
= \mathbf{0} .
\tag{15}
$$

By subtracting (15) from (14), and rearranging terms, we obtain the perturbation forward problem statement:

$$
\begin{bmatrix}
(\mathbf{I}+\mathbf{K})_{nn} & -\mathbf{V}_{nd} & -\mathbf{L}_{n\mu} \\
-\mathbf{K}_{dn} & \mathbf{V}_{dd} & \mathbf{L}_{d\mu} \\
-\mathbf{M}^*_{\mu n} & \mathbf{L}^*_{\mu d} & \mathbf{N}_{\mu\mu}
\end{bmatrix}
\begin{Bmatrix}
\delta\mathbf{u}_n \\
\delta\mathbf{f}_d \\
\boldsymbol{\mu}
\end{Bmatrix}
=
\begin{Bmatrix}
\mathbf{0} \\
\mathbf{0} \\
\boldsymbol{\lambda}_\mu
\end{Bmatrix} ,
\tag{16}
$$

where

$$
\delta\mathbf{u}_n = \mathbf{u}_n^{(D)} - \mathbf{u}_n^{(P)} ,
$$

$$
\delta\mathbf{f}_d = \mathbf{f}_d^{(D)} - \mathbf{f}_d^{(P)} ,
\tag{17}
$$

$$
\boldsymbol{\lambda}_\mu = \mathbf{M}^*_{\mu d}\boldsymbol{\phi} + \mathbf{M}^*_{\mu n}\mathbf{u}_n^{(P)} - \mathbf{L}^*_{\mu d}\mathbf{f}_d^{(P)} - \mathbf{L}^*_{\mu n}\boldsymbol{\psi} .
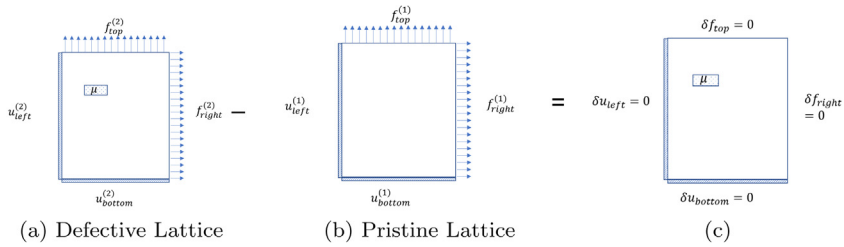$$

Fig. 6. Perturbation forward problem as the difference between two problems.
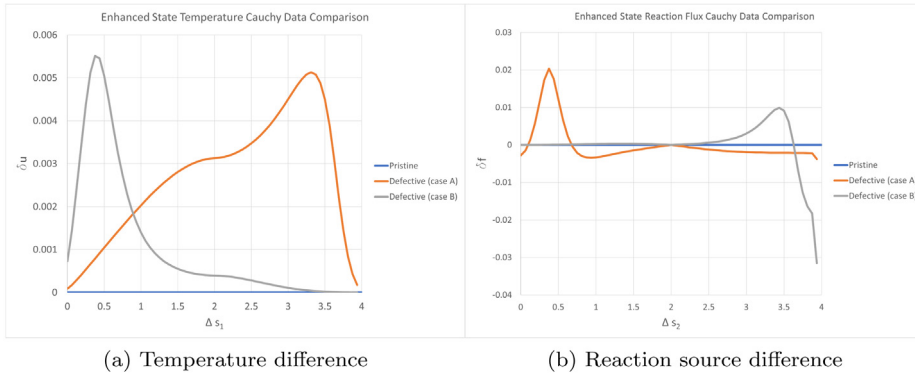

Fig. 7. Differences among the three lattices obtained by solving the perturbation forward problem (16). (For interpretation of the references to color in this figure legend, the reader is referred to the web version of this article.)

In effect, the column-vectors $\delta\mathbf{u}_n$ and $\delta\mathbf{f}_d$ capture the differences between the unknown Cauchy data for the defective and pristine lattice; the number of unknowns remains N_e. The expectation now is that the Cauchy data *differences* will prove to be more sensitive to defects than the original Cauchy data were. We note that similarly-cast perturbation problems have been often used for various problems in the mechanics of the continuum; they are of particular usefulness in inverse problems: see, for example, [19], where an approach based on differential measurements of far-field operators has been proposed for detecting defects embedded in an unknown host.

3.3. The motivational example revisited

Let us revisit the motivational example introduced in Section 3.1 using (16) rather (13). Accordingly, now we plot $\delta\mathbf{u}_n$ rather than $\mathbf{u}_n$, and $\delta\mathbf{f}_d$ rather than $\mathbf{f}_d$, along Δs_1 and Δs_2, respectively (Fig. 7). It is clear that differences among the lattices are now quite pronounced, much more so than in Fig. 5.

Based on results presented in Figs. 5 and 7, we proceed to analyzing the inverse problem for defective lattices using the perturbation (16) rather than the original forward problem formulation (13).

4. The inverse problem

As far as (16) is concerned, the inverse problem is to determine $\boldsymbol{\mu}$ in terms of prescribed Cauchy data, which include not only $\boldsymbol{\phi}$ and $\boldsymbol{\psi}$, but also some or all components of $\delta\mathbf{u}_n$ and/or $\delta\mathbf{f}_d$. This requires one to determine *both* $\boldsymbol{\mu}$ *and* the set of all defective bars $\mathcal{B}_\mu$: computing this set presents the most challenging aspect of the problem, and, consequently, our approach is significantly affected by this challenge.

4.1. Functionals

We cast the inverse problem within a model-constrained optimization framework [14], whereby the Lagrangian to be minimized consists of three terms, corresponding to the misfit, the forward problem side constraint, and the regularization functionals.

To formulate the misfit term, we rewrite (16) as:

$$
\begin{bmatrix} (\mathbf{I}+\mathbf{K})_{nn} & -\mathbf{V}_{nd} & \mathbf{0} \\ -\mathbf{K}_{dn} & \mathbf{V}_{dd} & \mathbf{0} \\ \mathbf{M}_{\mu n}^{*} & -\mathbf{L}_{\mu d}^{*} & \mathbf{I}_{\mu\mu} \end{bmatrix} \begin{Bmatrix} \delta\mathbf{u}_n \\ \delta\mathbf{f}_d \\ \boldsymbol{\lambda}_{\mu} \end{Bmatrix} = \begin{bmatrix} \mathbf{L}_{n\mu} \\ -\mathbf{L}_{d\mu} \\ \mathbf{N}_{\mu\mu} \end{bmatrix} \boldsymbol{\mu} .
\tag{18}
$$

This system of equations emphasizes that for any chosen $\boldsymbol{\mu}$, we can solve it for the column-vector

$$
\mathbf{b}_{\mathrm{p}} := \begin{Bmatrix} \delta\mathbf{u}_n \\ \delta\mathbf{f}_d \\ \boldsymbol{\lambda}_{\mu} \end{Bmatrix} = \begin{bmatrix} (\mathbf{I}+\mathbf{K})_{nn} & -\mathbf{V}_{nd} & \mathbf{0} \\ -\mathbf{K}_{dn} & \mathbf{V}_{dd} & \mathbf{0} \\ \mathbf{M}_{\mu n}^{*} & -\mathbf{L}_{\mu d}^{*} & \mathbf{I}_{\mu\mu} \end{bmatrix}^{-1} \begin{bmatrix} \mathbf{L}_{n\mu} \\ -\mathbf{L}_{d\mu} \\ \mathbf{N}_{\mu\mu} \end{bmatrix} \boldsymbol{\mu} := \mathbf{A}\boldsymbol{\mu} .
\tag{19}
$$

Here we use the subscript "p" to emphasize that the column-vector $\mathbf{b}_{\mathrm{p}}$ is predicted. On the other hand, if complete Cauchy data are prescribed and the set $\mathcal{B}_{\mu}$ is known, we can use (17) to compute $\mathbf{b}_{\mathrm{m}}$, where the subscript "m" implies that $\mathbf{b}_{\mathrm{m}}$ is in effect a measured, *a priori* known, column-vector. Thus, we can express the misfit functional $\mathfrak{L}_{\mathrm{M}}$ for $\boldsymbol{\mu}$ as

$$
\mathfrak{L}_{\mathrm{M}} := \left(\mathbf{b}_{\mathrm{p}} - \mathbf{b}_{\mathrm{m}}\right)^{T} \left(\mathbf{b}_{\mathrm{p}} - \mathbf{b}_{\mathrm{m}}\right) = \left(\mathbf{A}\boldsymbol{\mu} - \mathbf{b}_{\mathrm{m}}\right)^{T} \left(\mathbf{A}\boldsymbol{\mu} - \mathbf{b}_{\mathrm{m}}\right) .
\tag{20}
$$

Note that, for any chosen $\boldsymbol{\mu}$, $\mathfrak{L}_{\mathrm{M}}$ is constructed so that the forward problem stated in (16) is solved exactly. Therefore, the side constraint is satisfied exactly and the corresponding functional can be omitted.

The regularization functional adopted here is chosen so that it is capable of discriminating between defective and pristine bars. For this purpose, the standard $\ell_2(\boldsymbol{\mu})$ norm is not useful as it invites a broad spectrum of $\boldsymbol{\mu}$ values, which does not allow one to discriminate between defective and pristine bars. In contrast, the $\ell_1(\boldsymbol{\mu})$ norm is well-suited for our purposes [20,21]. For this reason, we define the Lagrangian $\mathfrak{L}$ in the form

$$
\mathfrak{L} := \mathfrak{L}_{\mathrm{M}} + R\|\boldsymbol{\mu}\|_1 = \left(\mathbf{A}\boldsymbol{\mu} - \mathbf{b}_{\mathrm{m}}\right)^{T} \left(\mathbf{A}\boldsymbol{\mu} - \mathbf{b}_{\mathrm{m}}\right) + R\|\boldsymbol{\mu}\|_1 ,
\tag{21}
$$

where R is a scalar regularization factor.

The Lagrangian in (21) is difficult to exploit as the matrix $\mathbf{A}$ cannot be computed without defining the trial set $\mathcal{B}_{\mu}$ *a priori*. Of course, one can start the inversion process by assuming that the set $\mathcal{B}_{\mu}$ is very large, potentially consisting of all lattice bars, but this will result in a prohibitively expensive problem size. To compensate, we devise a two-stage algorithm, where, at the first stage, we seek to reduce the size of the initial set $\mathcal{B}_{\mu}$, and, during the second stage, determine the actual $\mathcal{B}_{\mu}$ and the corresponding $\boldsymbol{\mu}$. The proposed algorithm structure can be easily explained. At the first stage, we disregard the fact that the defects are removed bars. That is, we disregard the equivalence relationship (6), and, ultimately, the last row in (16). Accordingly, we search for a set of dipoles to be placed in the pristine lattice that would match the measured data. This set of dipoles serves as the basis for identifying the trial set $\mathcal{B}_{\mu}$. At the second stage, we take into account that the defects have zero conductance, restore the last row in (16), and solve for $\boldsymbol{\mu}$ (and $\mathcal{B}_{\mu}$) using (21).

The forward problem corresponding to the first stage is derived from the first two rows of the block-matrix in (16). Accordingly, following (19), it is formulated as

$$
\mathbf{b}_{\mathrm{p}}^{*} := \begin{Bmatrix} \delta\mathbf{u}_n \\ \delta\mathbf{f}_d \end{Bmatrix} = \begin{bmatrix} (\mathbf{I}+\mathbf{K})_{nn} & -\mathbf{V}_{nd} \\ -\mathbf{K}_{dn} & \mathbf{V}_{dd} \end{bmatrix}^{-1} \begin{bmatrix} \mathbf{L}_{n\mu} \\ -\mathbf{L}_{d\mu} \end{bmatrix} \boldsymbol{\mu} := \mathbf{A}^{*}\boldsymbol{\mu} .
\tag{22}
$$

Note that the block-matrices in this equation are independent of $\mathcal{B}_{\mu}$, simply because here the dipoles are treated as ordinary rather than polarization ones. The Lagrangian corresponding to (22) is structured exactly as the one in (21), i.e.,

$$
\mathfrak{L}^{*} := \left(\mathbf{A}^{*}\boldsymbol{\mu} - \mathbf{b}_{\mathrm{m}}^{*}\right)^{T} \left(\mathbf{A}^{*}\boldsymbol{\mu} - \mathbf{b}_{\mathrm{m}}^{*}\right) + R\|\boldsymbol{\mu}\|_1 .
\tag{23}
$$

4.2. The first inversion stage

The first stage of the proposed algorithm involves minimization of $\mathfrak{L}^{*}$. This problem is closely related to a well-established problem in statistics: Least Absolute Shrinkage and Selection Operator (LASSO) [22]. To this end, we rewrite the minimization problem for the Lagrangian $\mathfrak{L}^{*}$ in the LASSO-consistent form

$$
\min_{\boldsymbol{\mu}} \mathfrak{L}^{*} \Leftrightarrow \operatorname*{argmin}_{\boldsymbol{\mu}\in\mathbb{R}^p} \left[\sum_{i=1}^{n} \left(\tilde{b}_i^{*} - b_0^{*} - \sum_{j=1}^{p} \tilde{A}_{ij}^{*}\mu_j \right)^2 + R\sum_{j=1}^{p} |\mu_j| \right] ,
\tag{24}
$$

where p is the total number of bars, and n is the number of available measurements. The column entries of the matrix $\tilde{\mathbf{A}}^*$ are computed as the mean-adjusted columns of $\mathbf{A}^*$:

$$\tilde{A}^*_{ij} = A^*_{ij} - \frac{1}{n} \sum_{k=1}^{n} A^*_{kj} \,. \tag{25}$$

Similarly, $\tilde{\mathbf{b}}^*$ is computed as the mean-adjusted column-vector of measurements $\mathbf{b}^*_m$:

$$\tilde{b}^*_i = (b^*_m)_i - \frac{1}{n} \sum_{k=1}^{n} (b^*_m)_k \,. \tag{26}$$

Finally, the intercept b^*_0 is computed as:

$$b^*_0 = \frac{1}{n} \sum_{k=1}^{n} \sum_{j=1}^{p} A^*_{kj} \mu_j - \frac{1}{n} \sum_{k=1}^{n} (b^*_m)_k \,. \tag{27}$$

For a fixed value of the regularization factor R, LASSO minimization reduces the inversion target $\boldsymbol{\mu}$, by forcing most of its components to zero, while allowing only a small number of non-zeros. This behavior is highly desirable as it indirectly treats the dipoles in a binary manner (zero and non-zero), consistent with the problem physics.

We note that the interplay between the misfit and regularization terms in (23) or (24) is rather important. In particular, for small R, the misfit would be dominant, likely leading to solutions for $\boldsymbol{\mu}$ corresponding to many bars with small, but non-zero, conductance. For large R, one would unduly emphasize the regularization term over the misfit, leading to a small $\mathcal{B}_\mu$, which may exclude some of the defective bars. In fact, as discussed below, the LASSO minimization algorithm for R larger than a critical value, is guaranteed to return an empty trial set $\mathcal{B}_\mu$, and, consequently, $\boldsymbol{\mu} = \mathbf{0}$.

To address the interplay between the misfit and regularization terms, we use a continuation scheme that seeks to balance the two terms of the Lagrangian. Specifically, once the minimization of $\mathfrak{L}^*$ is completed for a fixed R, during the second stage, we re-enlist the complete set of Eqs. (18) and attempt to minimize $\mathfrak{L}$ (instead of $\mathfrak{L}^*$), while also assessing whether the first-stage $\mathcal{B}_\mu$ and $\boldsymbol{\mu}$ satisfy (18). The second-stage algorithm will terminate successfully if and only if the trial set $\mathcal{B}_\mu$ contains all defective bars. If the second stage fails, this implies that the trial set $\mathcal{B}_\mu$ computed at the first stage did not contain all defective bars. Then, the first stage is restarted with a smaller value of the regularization factor R, so that the trial set $\mathcal{B}_\mu$ is enlarged. Note that the enlarged set is not guaranteed to be a superset of the sets corresponding to larger R values. The motivation for the regularization factor continuation scheme stems from the following theorem [23]:

Theorem 1. *If $R > R_{cr}$, then the minimizer of the LASSO functional* (24) *is $\boldsymbol{\mu} = \mathbf{0}$, where*

$$R_{cr} = \frac{1}{n} \left\| \tilde{\mathbf{A}}^{*T} \tilde{\mathbf{b}}^* \right\|_\infty \,. \tag{28}$$

This theorem guarantees that for any value of R greater than the critical R_{cr}, there are no solutions for $\boldsymbol{\mu}$ other than the trivial. Accordingly, we initiate the first stage with $R = \gamma R_{cr}$, and proceed to continuously decrease R based on the outcome of the second inversion stage. In our experience, $\gamma = 0.955$ is a good choice.

4.3. The second inversion stage

The polarization dipoles identified at the first stage are not required to represent zero-conductance bars. This is problematic for the minimization of $\mathfrak{L}$, because the trial set may include pristine bars, for which the equivalence condition (6) is inapplicable, and therefore (18) or (19) become invalid. We address this issue by assigning weights to the last N_μ equations of (19). Accordingly, the weighted form of the matrix $\hat{\mathbf{A}}$ is defined as:

$$\hat{A}_{ij} = A_{ij} \text{ for } i \in \mathcal{N}_e \text{ and } \hat{A}_{ij} = \sqrt{w_i} A_{ij} \text{ for } i \in \mathcal{B}_\mu \,, \tag{29}$$

where $\sqrt{w_i}$ denotes the ith equation weight. Similarly the measurements are weighted as

$$(\hat{b}_m)_i = (b_m)_i \text{ for } i \in \mathcal{N}_e \text{ and } (\hat{b}_m)_i = \sqrt{w_i}(b_m)_i \text{ for } i \in \mathcal{B}_\mu \,. \tag{30}$$
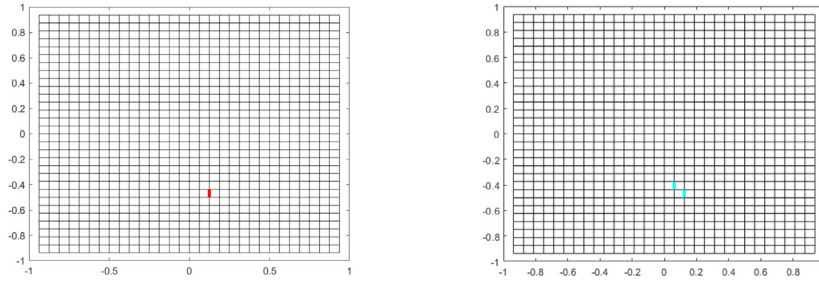
(a) Target defective lattice, with the defective bar shown in red color.

(b) The 2-bar trial set $\mathcal{B}_\mu$ shown in cyan color.

Fig. 8. The trial set $\mathcal{B}_\mu$ computed at the first stage. (For interpretation of the references to color in this figure legend, the reader is referred to the web version of this article.)

Consequently, the misfit term is modified, and, therefore, (20) is rewritten as

$$\hat{\mathfrak{L}}_{\mathrm{M}} := \left(\hat{\mathbf{b}}_{\mathrm{p}} - \hat{\mathbf{b}}_{\mathrm{m}} \right)^T \left(\hat{\mathbf{b}}_{\mathrm{p}} - \hat{\mathbf{b}}_{\mathrm{m}} \right) = \left(\hat{\mathbf{A}}\boldsymbol{\mu} - \hat{\mathbf{b}}_{\mathrm{m}} \right)^T \left(\hat{\mathbf{A}}\boldsymbol{\mu} - \hat{\mathbf{b}}_{\mathrm{m}} \right) . \tag{31}$$

Initially, all weights w_i are set equal to one. The weights are updated using the Iteratively Reweighted Least-Squares (IRLS) algorithm [24], until all weights converge to either zero or one. The IRLS algorithm updates the weights based on the residuals r_i after each Ordinary Least-Squares (OLS) solve; the residuals r_i, and their sum $\mathcal{R}_w$ are defined as

$$r_i = \sum_{j=1}^{N_e+N_\mu} \hat{A}_{ij}\mu_j - (\hat{b}_{\mathrm{m}})_i, \ i \in \mathcal{B}_\mu, \ \text{ and } \ \mathcal{R}_w = \sum_{i=1}^{N_\mu} |r_i| . \tag{32}$$

Equations with large residuals are progressively assigned smaller weights, until the weights converge. If the trial set $\mathcal{B}_\mu$ includes all defective bars, then the weights converge to one for those bars, and to zero for pristine bars in the trial set $\mathcal{B}_\mu$. Thus, (19) is satisfied for the defective bars, and the equivalence conditions for the pristine bars are discarded. In contrast, if the trial set $\mathcal{B}_\mu$ does not include all defective bars, then the weights converge to zero for the entire set. Thus, the termination condition of the second inversion stage was set as:

$$\mathcal{R}_w < \epsilon \text{ and } \|\mathbf{w}\|_1 > \epsilon , \tag{33}$$

where ϵ denotes a small tolerance. We note that the number of bars contained in the trial set $\mathcal{B}_\mu$ is usually relatively small, much smaller than the total number of bars, which makes the OLS solve computationally inexpensive.

To update the weights w_i, we use standardized adjusted residuals v_i, which are computed using the equation residuals r_i and leverages h_i. A leverage provides a metric for the sensitivity of the regression coefficients to the measured response after each OLS solve. Specifically, if $\mathbf{QR}$ is a factorization of $\hat{\mathbf{A}}$ into an orthogonal matrix $\mathbf{Q}$ and an upper-triangular matrix $\mathbf{R}$, so that the columns of $\mathbf{Q}$ span the range of $\hat{\mathbf{A}}$, then the leverages h_i are the diagonal elements of the projection matrix $\mathbf{H} = \mathbf{QQ}^T$. In statistics, the leverages allow one to identify outliers. In terms of the residual r_i for each equation, the standard deviation of error ϵ_{sd}, and the leverage h_i, the adjusted residuals are defined as

$$v_i = \frac{r_i}{c \, \epsilon_{\mathrm{sd}} \, \sqrt{1 - h_i}}, \tag{34}$$

where c is a tuning constant (we used $c = 4.685$ throughout), and ϵ_{sd} is estimated using the median absolute deviation of the residuals from their median [22,25].

Lastly, we used a bi-square weighting function that uses the standardized adjusted residuals v_i to update the weights according to

$$w_i = \begin{cases} (1 - v_i^2)^2 & \text{if } |v_i| < 1 \\ 0 & \text{if } |v_i| \geq 1 \end{cases} . \tag{35}$$

Failure to satisfy the second inversion stage termination condition (33) would imply that one or more defective bars are missing from the trial set $\mathcal{B}_\mu$. Then, the algorithm returns to the first stage with a smaller value for the regularization factor R, which would promote an enlarged set $\mathcal{B}_\mu$ during the first inversion stage. When all true defective bars are included in the trial set $\mathcal{B}_\mu$, the weights during the second stage will correctly identify the defective bars. The two-stage inversion algorithm is summarized in the following Algorithm:

Algorithm　Two-Stage Inversion for Localizing Lattice Defects

1: **procedure** TwoStageMinimizer
2:　　Set $\gamma = 0.955$ (Regularization factor R decrement)
3:　　Set $\epsilon = 10^{-10}$ (weighted OLS tolerance)
4:　　Set $R_{\min} = 0.01 R_{\mathrm{cr}}$　　　　　　　　　　　　　　　　　　　　　　▷ Theorem 1
5:　　Initialize polarization dipoles $\boldsymbol{\mu} = \mathbf{0}$
6:　　Initialize regularization factor $R = \gamma R_{\mathrm{cr}}$
7:　　**while** $R > R_{\min}$ **do**　　　　　　　　　　　　　　　　　　　▷ **First stage** LASSO loop
8:　　　　Minimize Lagrangian $\mathfrak{L}^*$, obtain $\boldsymbol{\mu}$　　　　　　　　　　　　　　　▷ Eq. (24)
9:　　　　Identify the trial set $\mathcal{B}_\mu$
10:　　　　Initialize IRLS weights $\mathbf{w} = \mathbf{1}$
11:　　　　Set $\mathcal{R}_w = 1 + \epsilon$
12:　　　　**while** ($\mathcal{R}_w > \epsilon$　&　$\|\mathbf{w}\|_1 > \epsilon$) **do**　　　　　　　▷ **Second stage** IRLS loop
13:　　　　　　Minimize $\hat{\mathfrak{L}}_{\mathrm{M}}$, obtain $\mathbf{w}, \boldsymbol{\mu}$
14:　　　　　　**if** $\|\mathbf{w}\|_1 > \epsilon$ **then**
15:　　　　　　　　$\mathcal{R}_w \leftarrow$ sum of weighted OLS residuals　　　　　　　　　▷ Eq. (33)
16:　　　　　　**else**
17:　　　　　　　　break
18:　　　　**end**
19:　　　　$R \leftarrow \gamma R$
20:　　**end**

---

5. Numerical experiments

In this section, we present results of four numerical experiments that were used to assess the efficacy of the two-stage inversion Algorithm in localizing lattice defects.

The first experiment involved lattices with a single removed bar. Specifically, we considered a lattice that occupied the square region $-1 \leq x \leq 1$ and $-1 \leq y \leq 1$, with a lattice spacing of $h = 1/16$. Accordingly, there are 128 boundary nodes ($N_e = 128$) and 1860 internal bars, and, consequently, the matrix $\mathbf{A}$, which was constructed using (19), has 128 rows and 1860 columns. We applied linearly varying temperatures along the bottom and left edges, and a unit source at every node along the right and top edges. This prescription realizes equal bi-linear temperature distribution in the pristine lattice. The single defective bar was located at $x = 2h$ and $8h \leq y \leq 9h$; it is indicated by red color in Fig. 8a.

First, we assumed that the complete Cauchy data were available; we refer to this case as the complete Cauchy data case. For the chosen data, (28) yielded $R_{\mathrm{cr}} = 6.82 \times 10^{-4}$. Since the decrement factor had been set to $\gamma = 0.955$, the first-stage LASSO solution started with $R = 6.51 \times 10^{-4}$, and concluded with the trial set $\mathcal{B}_\mu$, which included two bars: the actual defective bar and a pristine bar at $x = h$ and $9h \leq y \leq 10h$ (these bars are shown by cyan color in Fig. 8b). We note that the conductance of both bars was close to one: that is, at the end of the first stage, it was not possible to distinguish between the defective and pristine bars.

Next, the second stage was initiated with the 2-bar trial set $\mathcal{B}_\mu$. As the IRLS algorithm iteratively updated the weights, it ultimately assigned unit weight to the defective bar and zero weight to the pristine bar. Not surprisingly, the polarization dipole converged to the true value. Table 1 summarizes the results for both stages, and for both bars included in the trial set $\mathcal{B}_\mu$.

When a different single missing bar was selected, the result was equally successful. In short, in *all* cases of a single missing bar, under complete Cauchy data, the inversion algorithm successfully localized the defect.

Table 1
Polarization dipoles and conductances for the 2-bar trial set $\mathcal{B}_\mu$ shown in Fig. 8b.

Bar	First stage (LASSO)		Second stage (IRLS)	
	Dipole μ_j	Conductance c	Dipole μ_j	Conductivity c
1 (pristine)	0.0025	0.9608	0.0	1.0
2 (defective)	0.0764	0.9474	0.1249	0.0
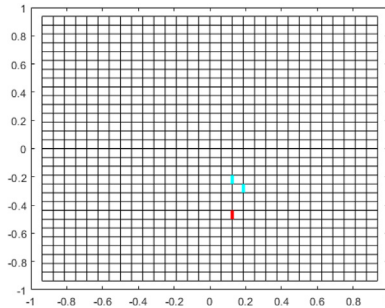
Fig. 9. The trial set $\mathcal{B}_\mu$ for the incomplete Cauchy data case. (For interpretation of the references to color in this figure legend, the reader is referred to the web version of this article.)
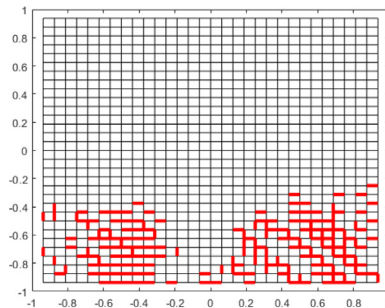
Fig. 10. Set of all single defective bars, shown in red, for which the first stage failed to produce a trial set $\mathcal{B}_\mu$ that included the defective bar (incomplete Cauchy data case). (For interpretation of the references to color in this figure legend, the reader is referred to the web version of this article.)

In the second set of numerical experiments, we restricted the availability of measurements to the top edge, while keeping the rest of the setting identical to the first set of numerical experiments; we refer to this set of experiments as the incomplete Cauchy data case.

In this case, the first stage produced a trial set $\mathcal{B}_\mu$ with 3 bars, which included two pristine bars and the true defective bar. The pristine bars are shown in Fig. 9 in cyan color, whereas the defective bar is shown in red color. In this particular case, the second inversion stage, initialized with the 3-bar trial set $\mathcal{B}_\mu$, successfully located the defective bar. We note though that when similarly incomplete Cauchy data were used to locate a different missing bar, the first-stage LASSO iterations were not always successful in including the true defective bar in the trial set. The set of all unsuccessful cases is captured pictorially by the red color bars in Fig. 10. Evidently, the algorithm was unsuccessful when the missing bar was sufficiently distant from the top edge, where the Cauchy data were prescribed.

The preceding experiments suggest that once the first stage produced a trial set $\mathcal{B}_\mu$ that included the true defective bar, the second stage would be able to correctly locate it, independently of the presence of pristine bars in the trial set. Thus, to better quantify the ability of the first stage to identify trial sets that are supersets of the true $\mathcal{B}_\mu$, for the third set of numerical experiment we chose to study the success rate of the first stage of the algorithm in including pairs of missing bars in the trial set, when complete Cauchy data were available. Since there are approximately 1.7 million possible pairs of bars, we chose a random sample of 1000 pairs, instead of exhaustively accounting

Table 2
Defect localization success rate for the complete Cauchy data for a random sample of 1000 pairs of missing bars.

Defect orientation	First-stage success rate	
	Single-state	Two-state
(v,h)	76.8%	99.1%
(v,v)	95.1%	94.1%
(h,h)	94.0%	94.9%

(a) Target void location   (b) $\mathcal{B}_\mu$ set of missing bars
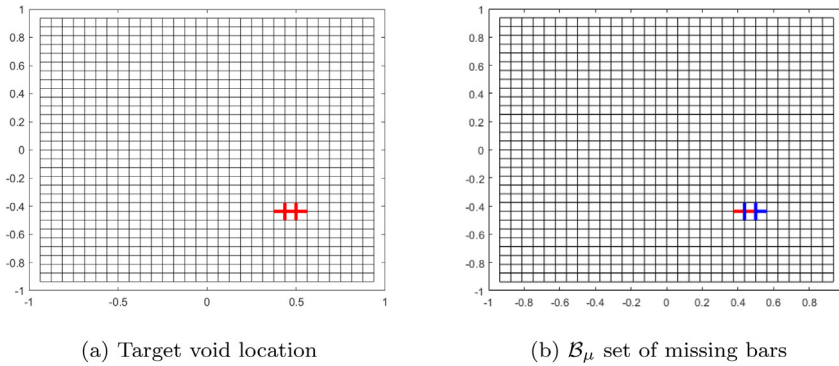
Fig. 11. Localization of a single void: (a) target void, realized by removing seven bars; (b) after the first inversion stage, the trial set $\mathcal{B}_\mu$ includes five of the missing bars. (For interpretation of the references to color in this figure legend, the reader is referred to the web version of this article.)

for all pairs. Unlike the single defective bar case, even for complete Cauchy data, the first-stage LASSO iterations were not always successful in including the pair in the trial set $\mathcal{B}_\mu$. The success rate is listed in Table 2 under the single-state case column. As it can be seen, the success rate was higher (and fairly high) when the two missing bars were both vertical ((v,v) orientation) or both horizontal ((h,h) orientation), than when the bars were of mixed orientation (v,h).

To improve on the ability of the algorithm to include the pair in the trial set, we subjected the lattice to two successive, instead of just one, thermal states, and then used the sum of the misfits defined over both states to drive the inversion. Thus, instead of a Cauchy data set obtained from a single bi-linear probing state, we used the combination of two Cauchy data sets, corresponding to two linear states, one in x and the other in y. Naturally, the unknown polarization dipoles doubled in number, since their magnitude (but not the set $\mathcal{B}_\mu$) was state-dependent. The success rate for the two-state case is also included in Table 2, showing remarkable improvement over the single-state case for pairs formed by one horizontal and one vertical bar.

For the fourth set of numerical experiments, we focused on a constellation of missing bars, forming a lattice void. Specifically, the synthetic void was created by removing seven bars within the region defined by $6h \leq x \leq 9h$ and $-8h \leq y \leq -6h$, as shown in Fig. 11a. Note that the forward problem for this void involves seven polarization dipoles, out of which only five are independent, because the sum of dipoles at the two interior nodes of the void must be equal to zero: this fact, as will be discussed, reduces the rank of $\tilde{\mathbf{A}}^*$ in (25), and may compromise the ability of the first-stage LASSO to include sufficient number of bars in the trial $\mathcal{B}_\mu$ set to lead to the localization of the true void.

To localize the void, we used measurements (complete Cauchy data) obtained from two linear thermal states of the lattice, and report successful void localization, for $R = 6.98 \times 10^{-4}$. We note that it was sufficient to identify only five out of seven defective bars during the first inversion stage: the 5-bar $\mathcal{B}_\mu$ set is shown in Fig. 11b.

As a variation of the fourth experiment, the synthetic void was moved towards the middle of the lattice, in the region defined by $-2h \leq x \leq h$ and $-2h \leq y \leq 0$, as shown in Fig. 12a. In this case, out of seven missing bars, the first-stage LASSO iterations returned a trial set $\mathcal{B}_\mu$ that included only four missing bars together with several pristine bars (see Fig. 12b; the regularization factor was $R = 3.91 \times 10^{-5}$). Since, for this particular void's
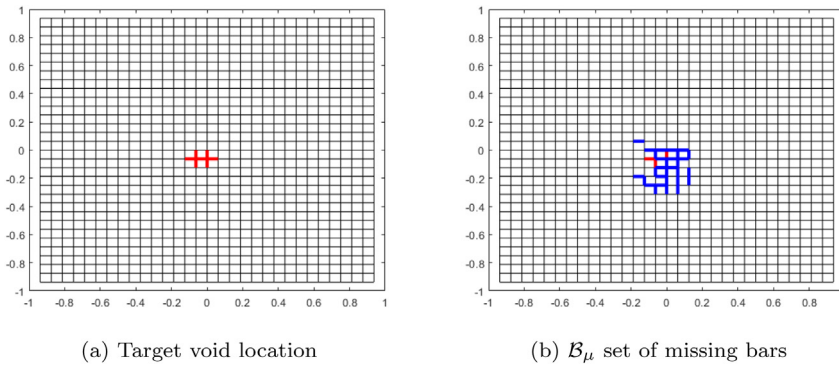
(a) Target void location   (b) $\mathcal{B}_\mu$ set of missing bars

Fig. 12. Localization of a single void in the middle of the lattice: (a) target void, realized by removing seven bars; (b) after the first inversion stage, the trial set $\mathcal{B}_\mu$ includes several pristine bars and only four of the missing bars. (For interpretation of the references to color in this figure legend, the reader is referred to the web version of this article.)

(a) Junction   (b) Loop
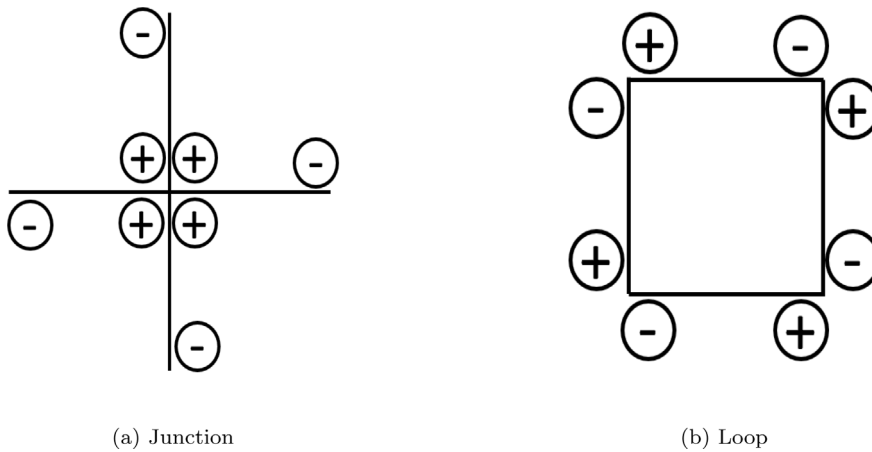
Fig. 13. Lattice bar topologies that lead to linear column dependence in the **L** matrices of (18).

geometry, at least five defective bars have to be included in the $\mathcal{B}_\mu$ set at the end of stage one, the second stage did not succeed in successfully localizing the void.

The difficulty with the first-stage LASSO iterations in the mid-lattice void case can be explained by examining the linear dependence structure of the **L** matrices in (18). Consider the bar configurations shown in Fig. 13 — a junction and a loop. The polarization dipoles are of the same magnitude and oriented as indicated by the circles with "positive" or "negative" signs. For each of these two configurations there are only three independent columns in the **L** matrices. The column dependence carries over to the matrix $\tilde{\mathbf{A}}^*$ in (25), and, as is known (e.g., [26]), exacerbates solution multiplicity, despite the ℓ_1 regularization.

A relatively straight-forward remedy is to use a linear combination of the ℓ_1 and ℓ_2 norms in the regularization term of (24); accordingly, the first inversion stage becomes:

$$\underset{\boldsymbol{\mu}\in\mathbb{R}^p}{\operatorname{argmin}}\left[\sum_{i=1}^{n}\left(\tilde{b}_i^* - b_0^* - \sum_{j=1}^{p}\tilde{A}_{ij}^*\mu_j\right)^2 + R\left\{\theta\sum_{j=1}^{p}|\mu_j| + (1-\theta)\sum_{j=1}^{p}\mu_j^2\right\}\right], \tag{36}$$

This generalization of LASSO minimization, commonly referred to as *elastic net minimization* in the statistics literature [22], introduces a new parameter θ that balances the ℓ_1 and ℓ_2 norm penalties: for θ close to 1.0, the elastic net solution is very similar to a LASSO solution except for bars that exhibit the aforementioned linear dependencies. In the latter case, elastic net chooses a maximal set of bars for the trial set $\mathcal{B}_\mu$. For example, using the elastic net Lagrangian of (36), the mid-lattice void of the previous numerical experiment was successfully
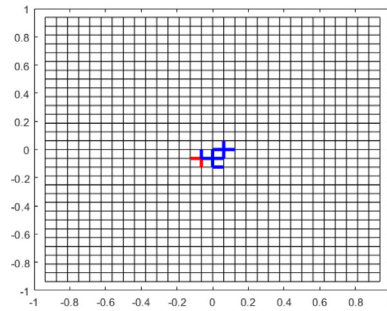
Fig. 14. Trial set $\mathcal{B}_\mu$ using elastic net minimization after first stage inversion ($R = 6.06 \times 10^{-4}$); five missing bars are included, leading to void localization. (For interpretation of the references to color in this figure legend, the reader is referred to the web version of this article.)
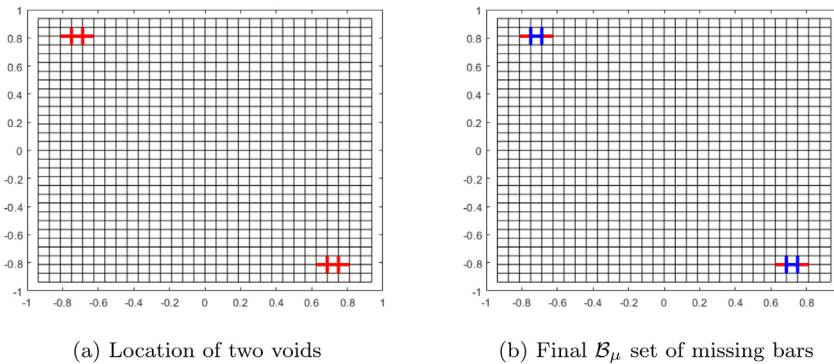

(a) Location of two voids   (b) Final $\mathcal{B}_\mu$ set of missing bars

Fig. 15. Localization of two voids: (a) target voids; (b) after the first inversion stage, the trial set $\mathcal{B}_\mu$ includes five of the missing bars for each void, leading to successful void localization. (For interpretation of the references to color in this figure legend, the reader is referred to the web version of this article.)

localized, since the $\mathcal{B}_\mu$ set included five out of the seven missing bars, as shown in Fig. 14. We also note that the modified first-stage elastic-net-based inversion (36), while useful for void localization, has no appreciable effect in the preceding experiments that involved either a single or a pair of missing bars. It has, thus, emerged as the preferred first-stage Lagrangian, since it is capable of localizing voids and groups of single-bar defects.

The last numerical experiment involved a lattice with two voids that are near symmetrically oriented about the diagonal of the lattice grid, as shown in Fig. 15. This lattice was probed using measurements from the two thermal states used in the experiments involving pairs of defective bars and single voids. The elastic net minimization was used in the first stage of inversion with $\theta = 0.95$. The algorithm successfully located both voids by including in the trial set $\mathcal{B}_\mu$ five out of seven bars for each void (Fig. 15b).

6. Closure

In this article, we developed an approach to the inverse problem of localizing removed bars in otherwise pristine lattices. First, with the aid of polarization dipoles, we showed that localizing the lattice defects is equivalent to solving an inverse source problem where the polarization dipoles become the inversion variables. This allowed us to operate always on the pristine lattice, without the need to modify the lattice grid during inversion iterations. Secondly, we devised a two-stage inversion algorithm with an embedded regularization factor continuation scheme that proved reasonably successful in localizing defects.

Although our overall approach followed standard ideas of model-constrained optimization, we had to address several aspects that arise naturally in discrete but not in continuum inverse problems. Perhaps the most significant of those issues is the identification of trial sets of bars that allow one to ultimately locate the actual defective bars. The proposed two-stage algorithm borrows elements from well-established methods in computational statistics (LASSO and elastic net), which were adapted to the lattice problem. Results of numerical experiments involving

single defective bars and pairs of defective bars suggest that the first-stage trial set must be a superset of the actual set of the defective bars $\mathcal{B}_\mu$ for the second-stage optimizer to successfully localize the defects. Results of numerical experiments involving voids revealed additional challenges due to the linear dependence of the equivalence conditions of the bars forming the void: to address the difficulty, we proposed a weighted regularization term that appeared to overcome the linear dependence and led to successful void localization, including cases involving well-separated voids.

Declaration of competing interest

Acknowledgments

References

[1] A. Nazir, K.M. Abate, A. Kumar, J.-Y. Jeng, A state-of-the-art review on types, design, optimization, and additive manufacturing of cellular structures, Int. J. Adv. Manuf. Technol. 104 (9) (2019) 3489–3510.

[2] M. Askari, D.A. Hutchins, P.J. Thomas, L. Astolfi, R.L. Watson, M. Abdi, M. Ricci, S. Laureti, L. Nie, S. Freear, R. Wildman, C. Tuck, M. Clarke, E. Woods, A.T. Clare, Additive manufacturing of metamaterials: A review, Addit. Manuf. 36 (2020) 101562.

[3] A. Álvarez-Trejo, E. Cuan-Urquizo, A. Roman-Flores, L. Trapaga-Martinez, J. Alvarado-Orozco, Bézier-based metamaterials: Synthesis, mechanics and additive manufacturing, Mater. Des. 199 (2021) 109412.

[4] J. Toivanen, V. Kolehmainen, T. Tarvainen, H. Orlande, J. Kaipio, Simultaneous estimation of spatially distributed thermal conductivity, heat capacity and surface heat transfer coefficient in thermal tomography, Int. J. Heat Mass Transfer 55 (25–26) (2012) 7958–7968.

[5] J. Toivanen, T. Tarvainen, J. Huttunen, T. Savolainen, H. Orlande, J. Kaipio, V. Kolehmainen, 3D thermal tomography with experimental measurement data, Int. J. Heat Mass Transfer 78 (2014) 1126–1134.

[6] V. Bakirov, R. Kline, W. Winfree, Discrete variable thermal tomography, in: AIP Conference Proceedings, Vol. 700, American Institute of Physics, 2004, pp. 469–476.

[7] E.B. Curtis, J.A. Morrow, The Dirichlet to Neumann map for a resistor network, SIAM J. Appl. Math. 51 (4) (1991) 1011–1029.

[8] P.-G. Martinsson, Fast Multiscale Methods for Lattice Equations (Ph.D. thesis), University of Texas at Austin, 2002.

[9] P.-G. Martinsson, G.J. Rodin, Asymptotic expansions of lattice Green's functions, Proc. R. Soc. Lond. Ser. A Math. Phys. Eng. Sci. 458 (2027) (2002) 2609–2622.

[10] P.-G. Martinsson, G.J. Rodin, Boundary algebraic equations for lattice problems, in: A.B. Movchan (Ed.), IUTAM Symposium on Asymptotics, Singularities and Homogenisation in Problems of Mechanics, 2002, pp. 191–198.

[11] S. Haq, A.B. Movchan, G.J. Rodin, Lattice Green's functions in nonlinear analysis of defects, J. Appl. Mech. 74 (4) (2007) 686–690.

[12] P.-G. Martinsson, G.J. Rodin, Boundary algebraic equations for lattice problems, Proc. R. Soc. Lond. Ser. A Math. Phys. Eng. Sci. 465 (2) (2009) 2489–2503.

[13] V. Bhamidipati, L.F. Kallivokas, G.J. Rodin, Green's analysis of conducting lattices, J. Eng. Math. (2021).

[14] J.-L. Lions, Optimal Control of Systems Governed By Partial Differential Equations, Vol. Bd. 170;Bd. 170, Springer-Verlag, 1971.

[15] S.-W. Na, L.F. Kallivokas, Partial-differential-equation-constrained amplitude-based shape detection in inverse acoustic scattering, Comput. Mech. 41 (4) (2008) 579–594.

[16] A. Fathi, L.F. Kallivokas, B. Poursartip, Full-waveform inversion in three-dimensional PML-truncated elastic media, Comput. Methods Appl. Mech. Engrg. 296 (2015) 39–72.

[17] T. Bui-Thanh, O. Ghattas, A PDE-constrained optimization approach to the discontinuous Petrov-Galerkin method with a trust region inexact Newton-CG solver, Comput. Methods Appl. Mech. Engrg. 278 (2014) 20–40.

[18] J. Cserti, Application of the lattice Green's function for calculating the resistance of an infinite network of resistors, Amer. J. Phys. 68 (10) (2000) 896–906.

[19] L. Audibert, G. Alexandre, H. Haddar, Identifying defects in an unknown background using differential measurements, Inverse Probl. Imaging 9 (3) (2015) 625–643.

[20] E.J. Candés, M.B. Wakin, S.P. Boyd, Enhancing sparsity by reweighted ℓ_1 minimization, J. Fourier Anal. Appl. 14 (5) (2008) 877–905.

[21] S.-J. Kim, K. Koh, M. Lustig, S. Boyd, D. Gorinevsky, An interior-point method for large-scale ℓ_1-regularized least squares, IEEE J. Sel. Top. Sign. Proces. 1 (4) (2007) 606–617.

[22] T. Hastie, R. Tibshirani, J. Friedman, The Elements of Statistical Learning : Data Mining, Inference, and Prediction, second ed., in: Springer Series in Statistics, Springer, 2009.

[23] P. Bühlmann, S. Van De Geer, Statistics for High-Dimensional Data: Methods, Theory and Applications, Springer Science & Business Media, 2011.

[24] P.W. Holland, R.E. Welsch, Robust regression using iteratively reweighted least-squares, Comm. Statist. Theory Methods 6 (9) (1977) 813–827.

[25] W.J.J. Rey, Introduction to Robust and Quasi-Robust Statistical Methods, in: Universitext, Springer-Verlag, 1983.

[26] R.J. Tibshirani, et al., The LASSO problem and uniqueness, Electron. J. Stat. 7 (2013) 1456–1490.